Supporting information

Stabilizing Defects in Metal-Organic Frameworks: Pendant Basic Sites as Capping Agents in UiO-66-type MOFs toward Highly Stable and Defective Porous Materials

Caleb D. Fast,[a†] Jason Woods,[a] Jared Lentchner,[a] and Tegan A. Makal*[a]

[a] *Department of Natural Sciences, The University of Virginia's College at Wise, 1 College Avenue, Wise, VA 24293, United States*

[†] Current address: Department of Chemistry, Vanderbilt University, Nashville, TN 37235, United States

Table of Contents

A. Overview of MOF Synthesis

Table S1 Synthetic conditions for preparation of MOFs studied.

Name	*$ZrCl_4$*	*Acid modulator*	*Volume DMF*	*Mass H_2BDC-R*	*Temperature*	*Time in oven*
UiO-66	132 mg (0.566 mmol)	HCl (1 mL)	15 mL	130 mg (0.782 mmol)	85 °C	12 h
UiO-2OH	134 mg (0.575 mmol)	HCl (1 mL)	15 mL	150 mg (0.503 mmol)	85 °C	12 h
UiO-2SH	100 mg (0.429 mmol)	HOAc (3.72 mL)	16 mL	145 mg (0.629 mmol)	75 °C	12 h
UiO-SMe	117 mg (0.502 mmol)	HCl (1 mL)	13.5 mL	100 mg (0.471 mmol)	85 °C	12 h
UiO-2SEtSMe	84 mg (0.36 mmol)	HOAc (0.6 mL)	4 mL)	90 mg (0.23 mmol)	110 °C	48 h

B. PXRD Data

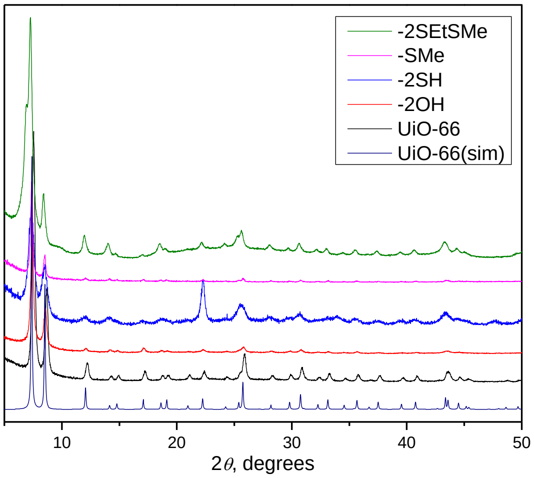

Figure S1 PXRD patterns of as-synthesized UiO-66-type MOFs studied compared to the simulated PXRD pattern of UiO-66 (denoted UiO-66(sim)). Simulated PXRD pattern generated using the Mercury software package with λ = 1.54 Å.

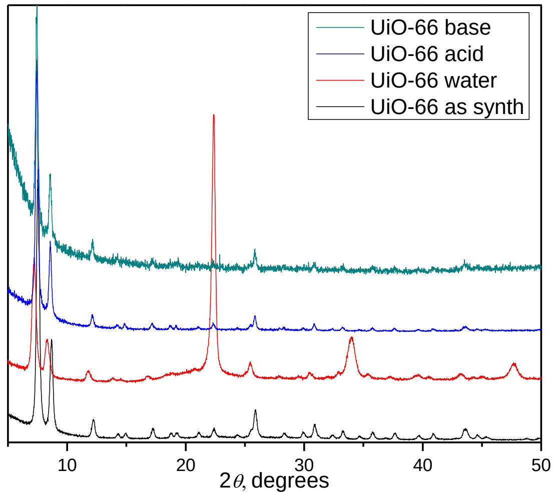

Figure S2 PXRD patterns of UiO-66 under a variety of conditions.

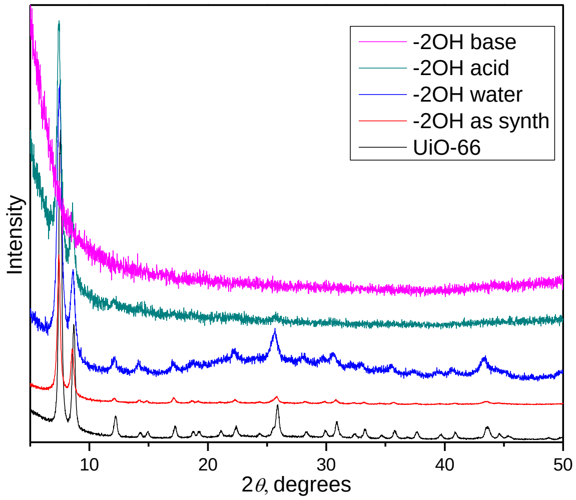

Figure S3 PXRD patterns of UiO-66-2OH under a variety of conditions compared to UiO-66-as.

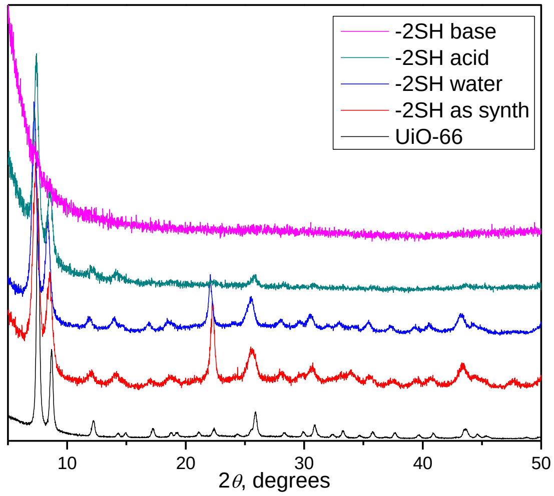

Figure S4 PXRD patterns of UiO-66-2SH under a variety of conditions compared to UiO-66-as.

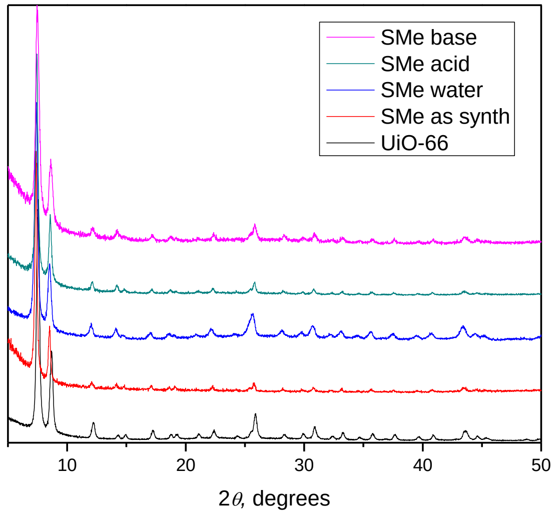

Figure S5 PXRD patterns of UiO-66-SMe under a variety of conditions.

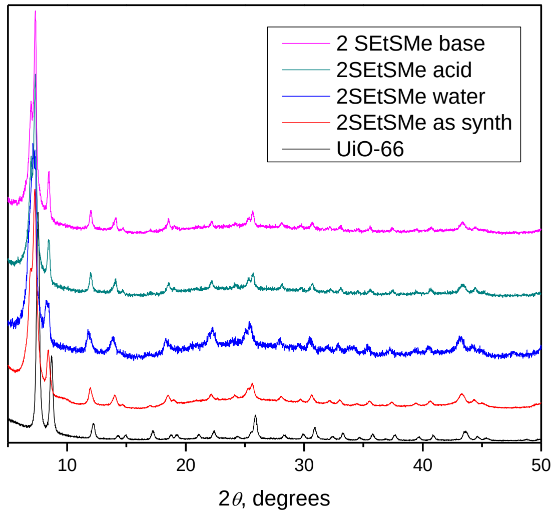

Figure S6 PXRD patterns of UiO-66-2SEtSMe under a variety of conditions.

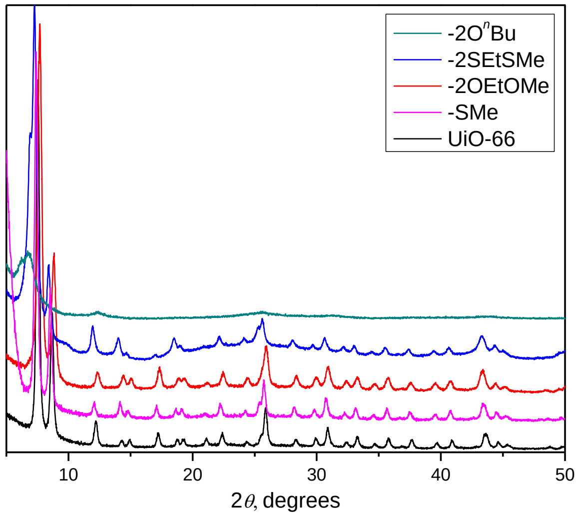

Figure S7 PXRD patterns of as-synthesized forms of UiO-66, UiO-66-SMe, UiO-66-2OEtOMe, UiO-66-2SEtSMe, and the solid formed from solvothermal synthesis involving $ZrCl_4$ and H_2BDC-2O^{n}Bu under the same conditions that UiO-66-2SEtSMe and -2OEtOMe were prepared.

C. TGA Data

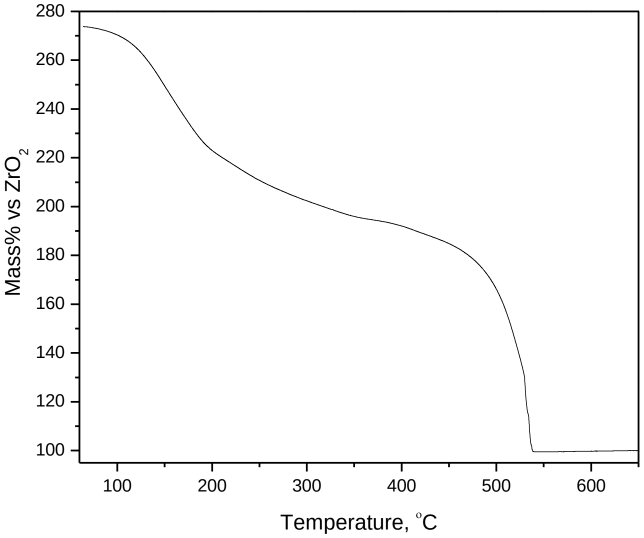

Figure S8 TGA curve for UiO-66

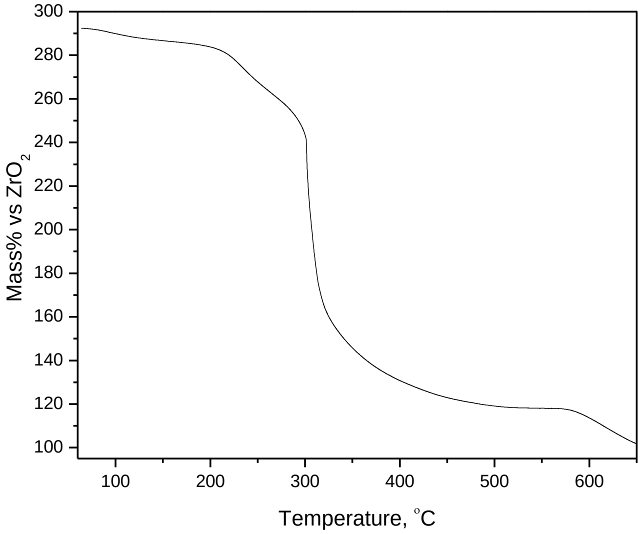

Figure S9 TGA curve for UiO-66-2OH

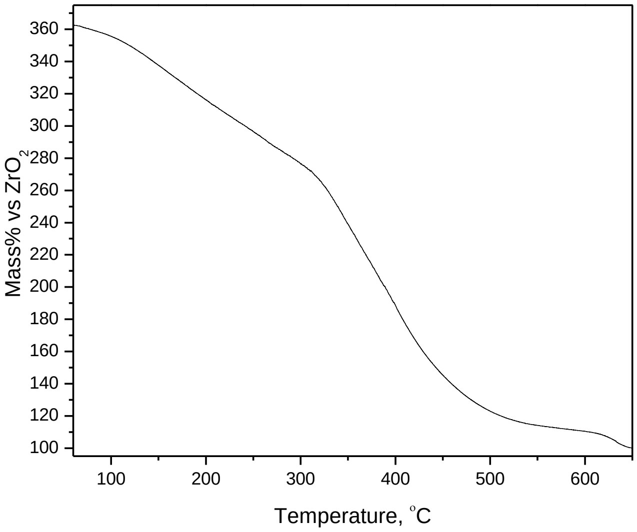

Figure S10 TGA curve for UiO-66-2SH

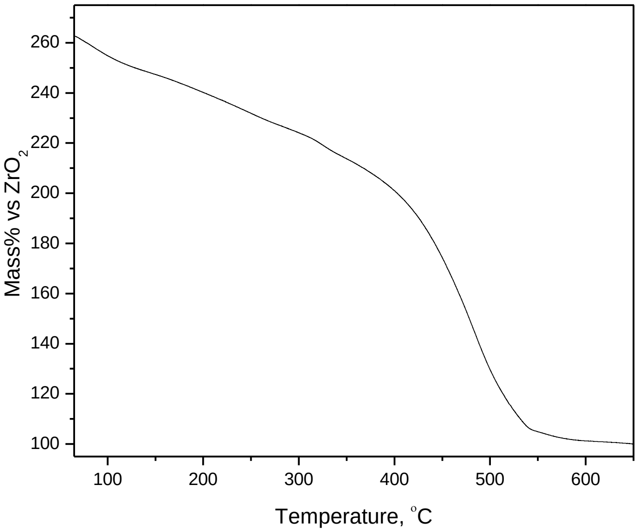

Figure S11 TGA curve for UiO-66-SMe

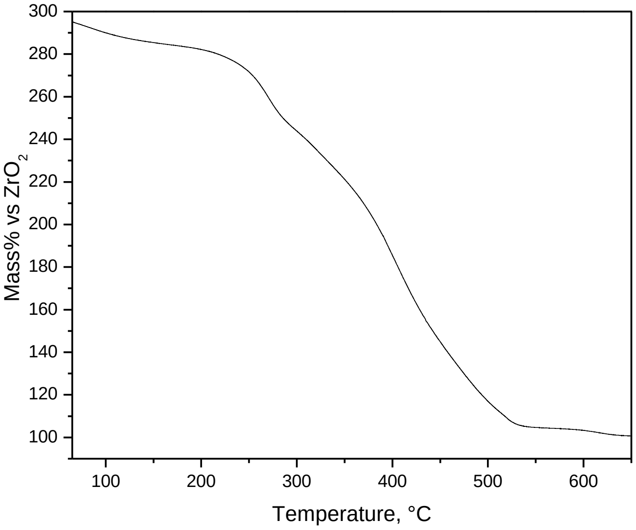

Figure S12 TGA curve for UiO-66-2SEtSMe

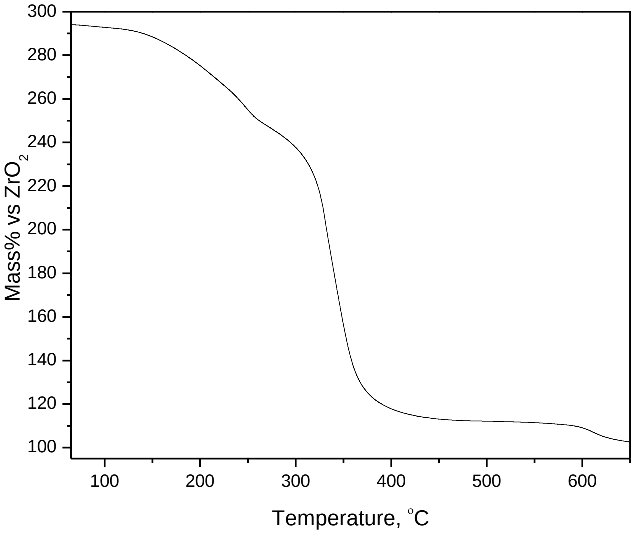

Figure S13 TGA curve for UiO-66-2OEtOMe

Table S2 Pertinent data related to determination of number of ligand defects in UiO-66-R MOFs.

	UiO-66	OH	SH	SMe	SEtSMe,L[a]	SEtSMe,H[a]	OEtOMe,L[a]	OEtOMe,H[a]
ZrO_2 mass%	100	100	100	100	100	100	100	100
Exptl dehyd. mass%[b]	191	240	270	210	218	250	235	250
T of dehyd., °C[c]	408	301	314	370	356	285	305	262
Ideal dehyd. mass%[d]	220.2	246.2	272.2	257.6	392.6	392.6	340.4	340.4
Ligands/fu[e]	4.54	5.75	5.92	4.19	2.42	3.08	3.37	3.74
Defects/fu[f]	1.46	0.25	0.08	1.81	3.58	2.92	2.63	2.26
%Defects	24.29	4.24	1.28	30.20	59.67	48.74	43.84	37.60
Dehyd. mass%, theor. w/ defects[g]	191.00	239.97	270.04	210.00	217.99	249.99	235.02	250.02

[a] When the TGA curve did not result in a clear plateau for the dehydrated MOF, an estimation of the number of ligand defects was determined by calculation of ligand defects in a "low-connectivity regime" and "high-connectivity regime", denoted by "xx,L" and "xx,H", respectively, where "xx" denotes the label for the specific MOF. In these instances, the low-connectivity regime is determined by taking the mass% immediately before the final large phenomena attributed to ligand combustion, whereas the high-connectivity regime is determined by taking the mass% immediately following the phenomena occurring before this final step, as determined from the first derivative plot of the TGA curve.

[b] Exptl dehyd. mass% = the mass% taken as that of the MOF after solvent removal and dehydration of the $Zr_6(OH)_4O_4$ SBU to produce the Zr_6O_6 SBU, and prior to combustion of the organic portion of the MOF, taken from the experimental TGA curve.

[c] T of dehyd. = the temperature at which the exptl dehyd. mass% was taken.

[d] Ideal dehyd. mass% = the theoretical mass% of the desolvated and dehydrated MOF if no defects are present.

[e] Ligands/fu = experimentally determined average number of ligands per formula unit. Calculated by:

$$\frac{Ligands}{fu} = \frac{Exptl\ dehyd. mass\% - Final\ mass\%}{Ideal\ dehyd. mass\%}$$

[f] Defects/fu = experimentally determined average number of ligand defects per formula unit. Calculated by:

$$\frac{Defects}{fu} = 6 - \left(\frac{Ligands}{fu}\right)$$

[f] Dehyd. mass%, theor. w/ defects = the theoretical mass% of the desolvated and dehydrated MOF calculated using the number of ligand defects determined and balancing the charge of missing ligands with oxide.

$$mass\%_{dehyd,theor,defects} = \frac{x*MW_L+(6+(6-x))*15.999+6*91.224}{(6*123.218)} * 100\%, x = \frac{ligands}{fu}, MW_L = molar\ mass\ of\ the\ ligand.$$

D. Experimental N_2 Sorption Isotherms

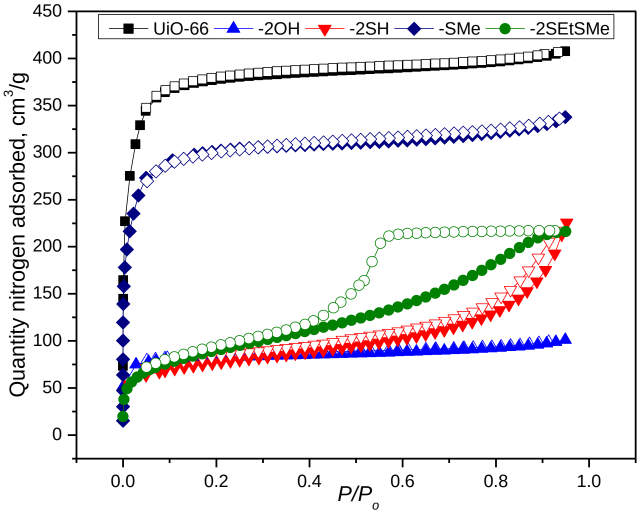

Figure S14 N_2 sorption isotherms collected at 77 K. Filled symbols = adsorption, empty symbols = desorption.

Table 3 BET and Langmuir surface areas for studied UiO-66-R MOFs as determined from N_2 sorption measurements at 77 K.

	UiO-66	UiO-66-2OH	UiO-66-2SH	UiO-66-SMe	UiO-66-2SEtSMe
BET surface area (m^2/g)	1129	276	606	938	301
Langmuir surface area (m^2/g)	1761	431	945	1463	380

E. Metal Uptake Results

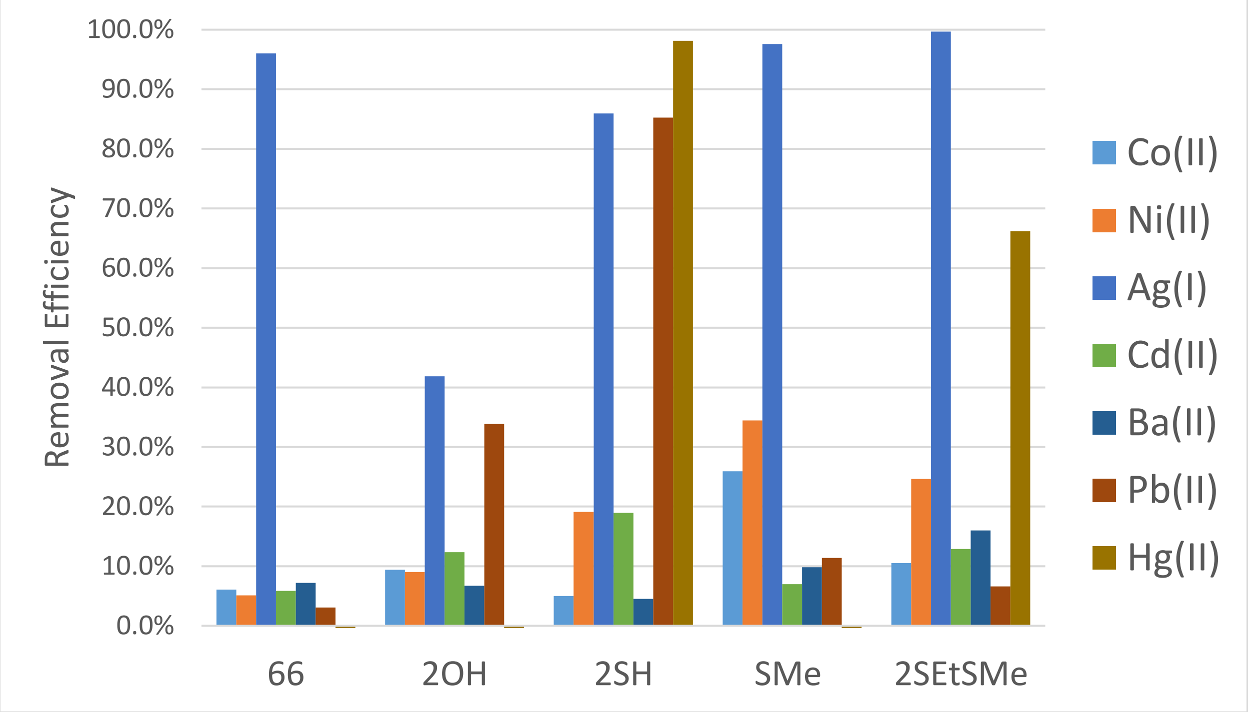

Figure S15 Removal efficiency of UiO-66 and UiO-66-R MOFs for M^{n+} in acidic (pH = 2) aqueous solutions. Removal efficiency is defined by C_f/C_i*100%, where C_f = equilibrium concentration after exposure to MOF, and C_i = concentration prior to exposure to MOF.

F. IR Spectra

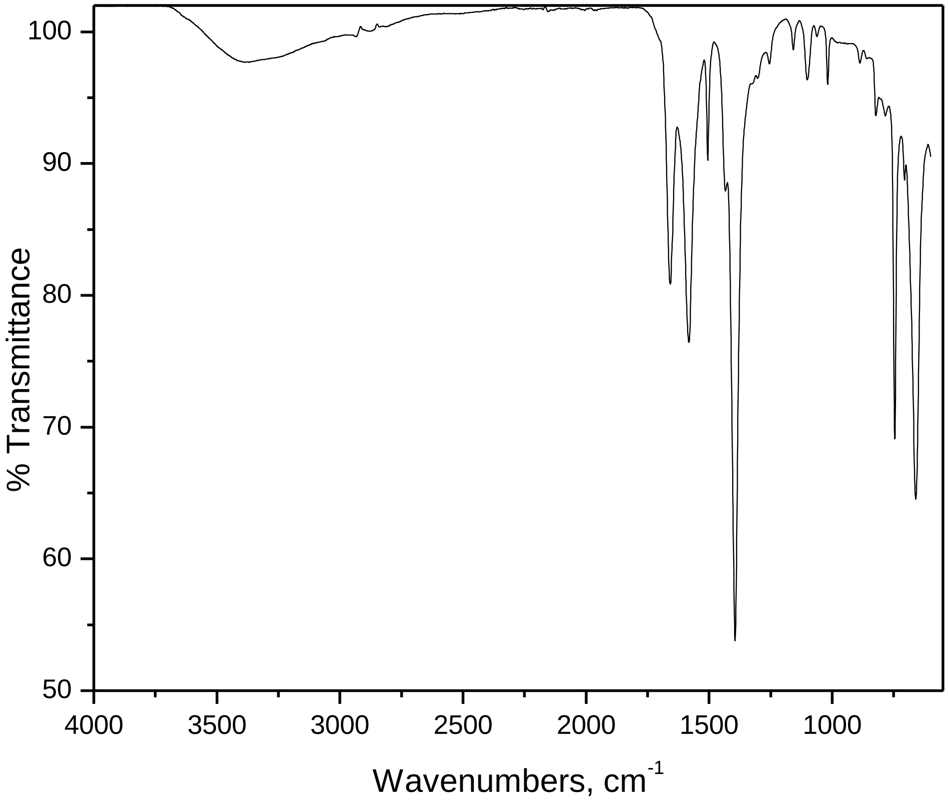

Figure S16 IR spectrum of UiO-66.

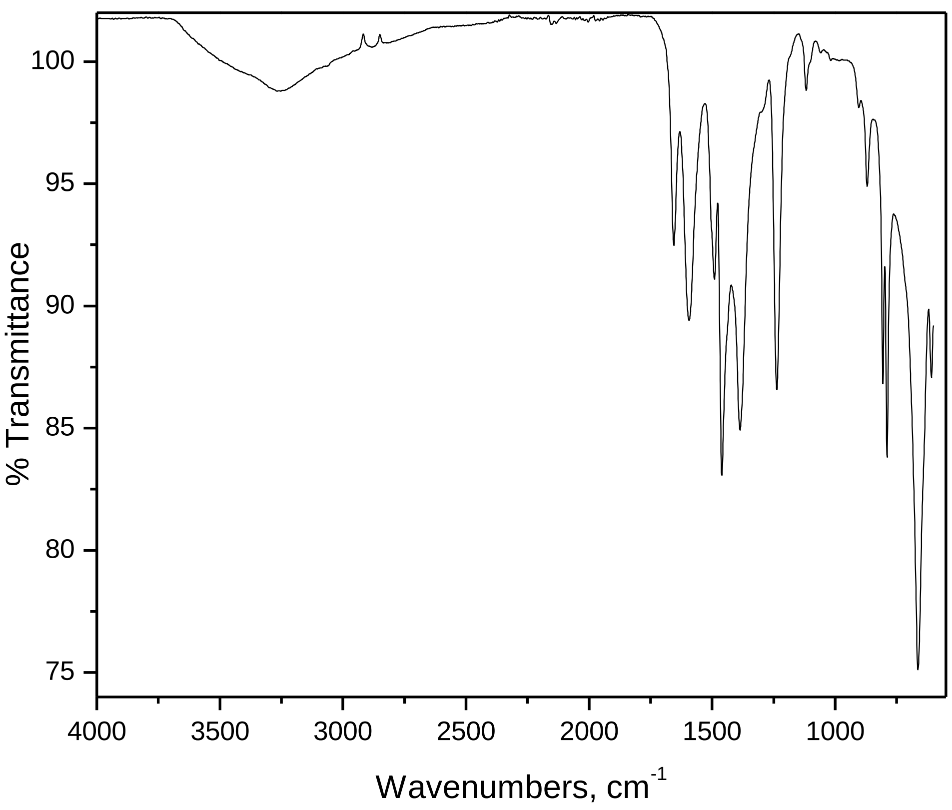

Figure S17 IR spectrum of UiO-66-2OH

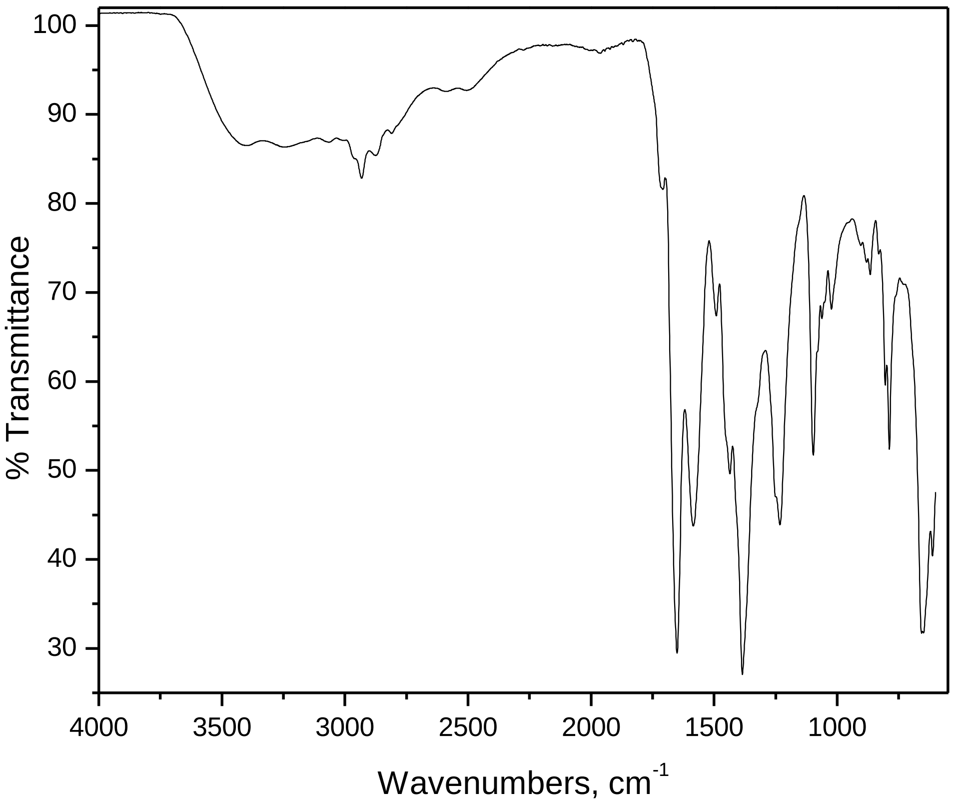

Figure S18 IR spectrum of UiO-66-2SH.

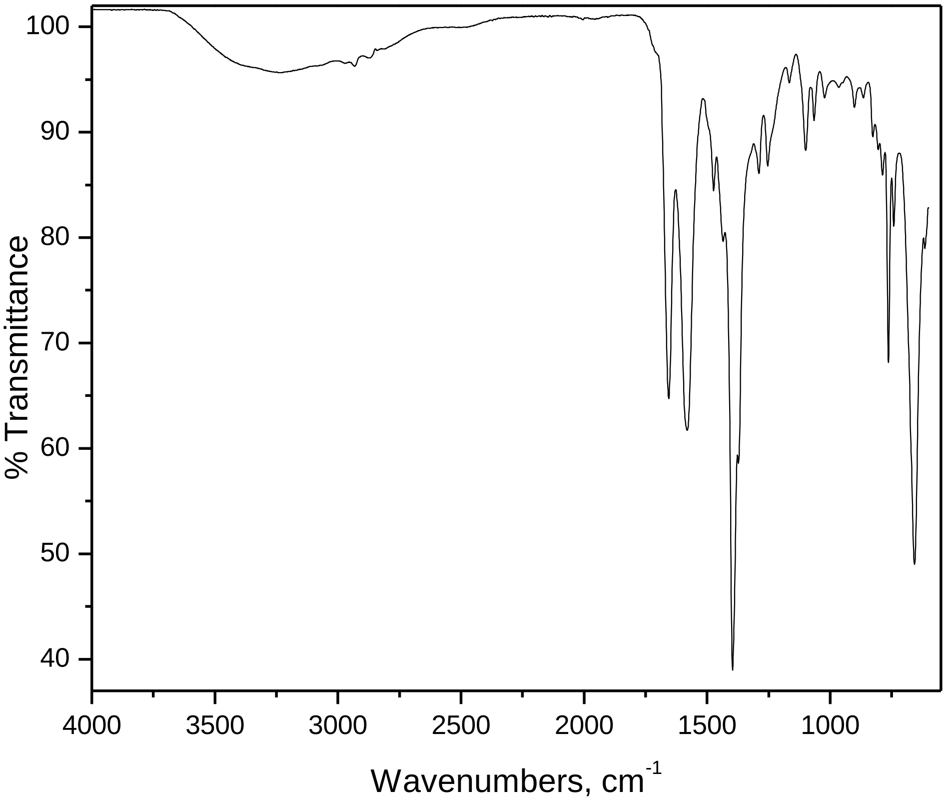

Figure S19 IR spectrum of UiO-66-SMe

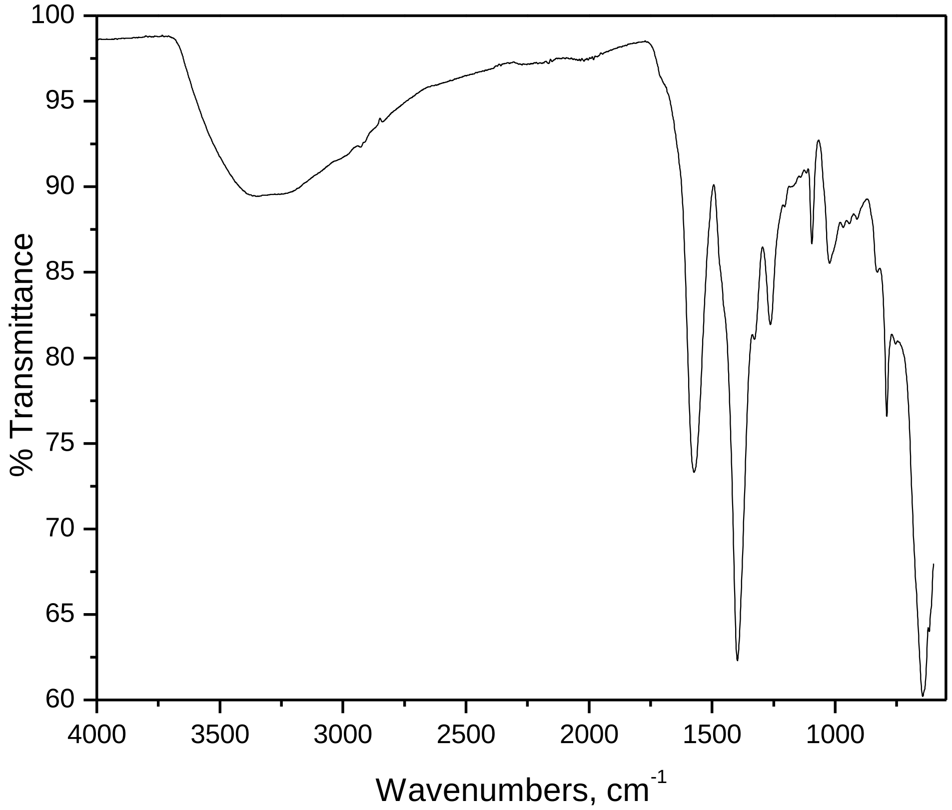

Figure S20 IR spectrum of UiO-66-2SEtSMe.

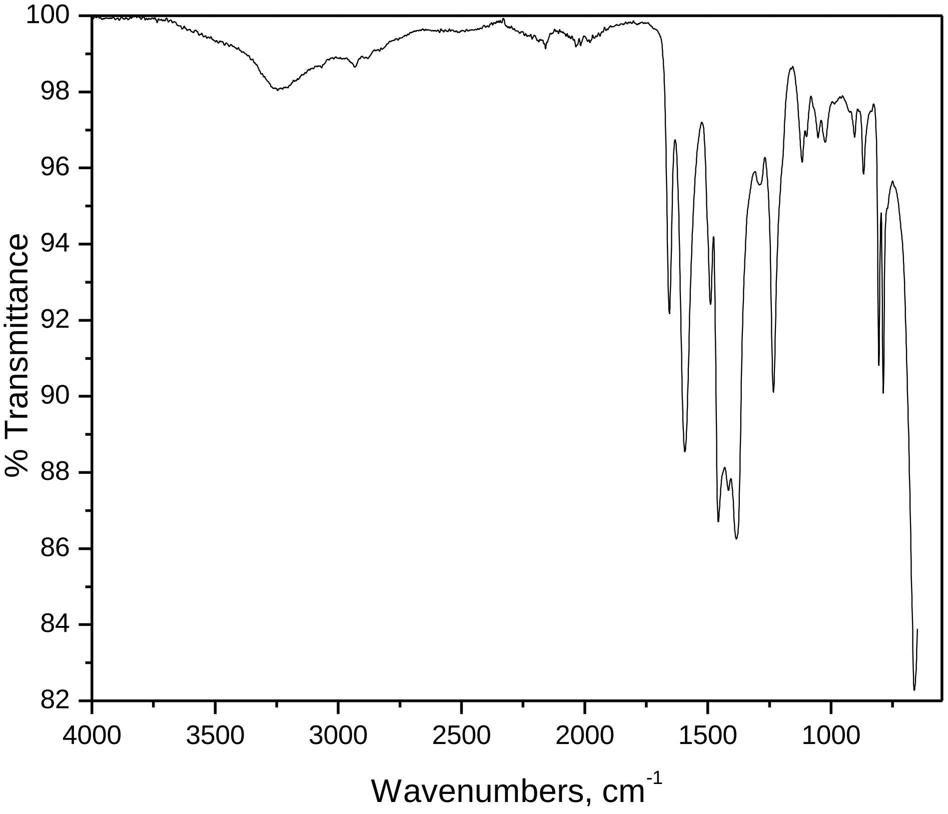

Figure S21 IR spectrum of UiO-66-2OEtOMe